Extreme Tribological Characteristics of Copolymers Induced by Dynamic Rheological Instability

Ara Kim<sup>1</sup>, Sinan Müftü<sup>2</sup>, Edwin L. Thomas<sup>3</sup>, Jae-Hwang Lee<sup>1,\*</sup>

<sup>1</sup>Department of Mechanical and Industrial Engineering, University of Massachusetts, Amherst,

Massachusetts 01003, United States

<sup>2</sup> Department of Mechanical and Industrial Engineering, Northeastern University, Boston,

Massachusetts 02139, United States

<sup>3</sup> Department of Materials Science and Engineering, Texas A&M University, College Station,

Texas 77843, United States

Corresponding author email: leejh@umass.edu

KEYWORDS: High-strain-rate, angled collision, friction, adhesion, additive manufacturing

Abstract

Nonlinear tribological behavior of polymeric microparticles under extreme collision conditions is required for in-depth understanding of advanced applications in the fields of defense, biomedicine,

and manufacturing. Laser-induced projectile impact tests with incidence angle of 45 degrees are

conducted to investigate the tribological response at the contact interface of block-copolymers

with glassy-rubbery phases and a stationary substrate to induce deformations with ultra-high

strain rate. Morphological-phase-dependent tribological and rheological responses are quantified

from the mechanical interactions involving adiabatic heating, plastic flow, and interfacial shear

1

instability. An effective coefficient of friction mechanism that depends on the rheological transition activated by impact velocity is proposed to specify the rheological response of the copolymers.

### 1. Introduction

Tribological phenomena, such as friction, wear, and adhesion, that occur when two materials move in relative contact are ubiquitous in daily life.<sup>1,2</sup> However, tribological interactions are generally very complex as they originate from multiscale physical interactions spanning a great range of temporal and spatial scales.<sup>3</sup> In certain cases, these interactions can be profoundly altered even by a monolayer of molecules at the interface, as they are predominantly related to interfacial properties between materials.<sup>4,5</sup> While a material's rate-dependent properties play an important role in the phenomena, the feedback between the energy dissipation by friction and the temperature-dependent material characteristics often creates tribological and rheological nonlinearities particularly under ultrahigh rate (UHR) conditions simultaneously accompanied by ultrahigh-strain-rates and very large strains. The nonlinear tribological and rheological characteristics of polymers are important for ballistic, biomedical, aerospace, and other applications. Moreover, the tribological interaction and adhesion at the contact interfaces over a wide range of strain rates are especially crucial to volatile organic compound (VOC) free additive manufacturing methods such as cold spray, 9-11 which enable solid-state consolidation of polymer powders through UHR plastic deformation and material fusion occurring in supersonic collisions between feedstock powders and a substrate.

Due to low phase transition temperatures and rate-dependent dynamics of macromolecules, the UHR tribological and rheological properties of polymers can exhibit exceptionally diverse nonlinearities and to date are not well understood. When a polymer micro-particle (μP) collides with a stationary target substrate, its kinetic energy is converted to heat due to adiabatic shock compression<sup>12</sup> and plastic deformation within a short duration (<100 ns). Combined with the low thermal conductivity of polymers, high-speed collision of polymeric μPs leads to an effectively adiabatic situation, which leads to the tribological nonlinearity of the material at the interface. To elucidate the UHR tribological behavior of polymer μPs under this extreme condition, we apply the laser-induced projectile impact test (LIPIT), <sup>11,13–15</sup> which can be used to achieve highly controlled impact of single μPs. In this work, we introduce the *angled laser-induced projectile* 

impact test ( $\theta$ -LIPIT) for the first time, where an off-normal incidence angle is used to quantify the extreme interfacial interaction of  $\mu$ Ps.

## 2. Results and Discussion

As model materials, polystyrene homopolymer (PS83) and two polystyrene-blockpolydimethylsiloxane (PS-b-PDMS) block copolymers (BCPs) PS87-PDMS40 and PS83-PDMS83 are selected. The number average molecular weight ( $\overline{M}_n^{PS}$ ) of the PS83 is 83 kg·mol<sup>-1</sup> while the PS87-PDMS40 consists of two blocks with  $\overline{M}_n^{PS} = 87$  and  $\overline{M}_n^{PDMS} = 40 \text{ kg} \cdot \text{mol}^{-1}$  and PS83-PDMS83 consists of two blocks with  $\overline{M}_n^{PS} = 83$  and  $\overline{M}_n^{PDMS} = 83 \text{ kg} \cdot \text{mol}^{-1}$ . Toluene, a nearneutral solvent was used to make (9.1 % wt) solutions of the polymers. These solutions were then sprayed into a hot air column ( $T = 125 \pm 5$ °C) using an ultrasonic atomizer (Fig. S1) and subsequently solidified into spherical µPs<sup>16</sup> with a range of diameters between 10 to 30 µm after 1 meter of free fall in the column (Fig. 1a). Unlike the amorphous state of PS83, due to the microphase separation of PS and PDMS domains during the solidification stage, PS87-PDMS40 and PS83-PDMS83 have distinctive nanoscale morphologies (Fig. 1c-1d). Based on volume fraction of PDMS (fPDMS), the morphologies of PS87-PDMS40 (fPDMS~30%) and PS83-PDMS83  $(f^{\text{PDMS}} \sim 50\%)$  would be expected as cylindrical PDMS domains in a PS matrix and lamellar morphologies respectively.<sup>17</sup> However, due to the rapid loss of solvent from the small particles, resulting in a very short time for microphase separation, the morphologies show only short-range ordering. As a target substrate, fused silica is primarily used as a rigid surface to ensure negligible plastic deformation on a substrate.

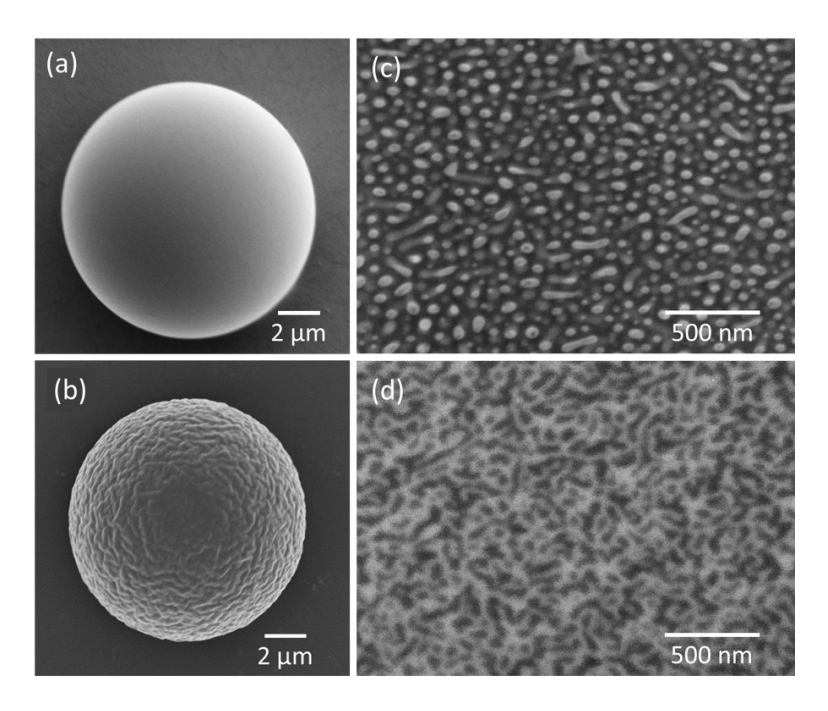


**Figure 1.** Scanning electron microscopy (SEM) image of (a) PS83 and (b) PS83-PDMS83 μPs. Cross-sectional SEM images of (c) PS87-PDMS40 and (d) PS83-PDMS83 μPs, where the brighter regions are PDMS. Sample PS87-PDMS40 shows discrete PDMS domains in a PS matrix, while PS83-PDMS83 shows a PDMS continuous matrix with both discrete and connected PS domains.

In  $\theta$ -LIPIT, a single polymer  $\mu P$  is accelerated to a broad range of velocities between 50 and 700 m·s<sup>-1</sup> using the rapid expansion of an elastomer film powered by laser ablation of an underlying gold thin-film (**Fig. 2a**). During the flight of the  $\mu P$ , a stroboscopic image is captured (**Fig. 2b**) with ultrafast white light pulses (< 1ps). Because  $\mu P$  impacts the stationary and rigid surface at a large angle ( $\theta_i \cong 45^\circ$ ), two components of initial velocity,  $v_{i,n}$  and  $v_{i,t}$  and the components of rebound velocity,  $v_{r,n}$  and  $v_{r,t}$  can be simultaneously measured along the surface normal and parallel vectors,  $\hat{n}$  and  $\hat{t}$ , respectively. While  $v_{i,n}$  and  $v_{r,n}$  represent the compression-dominant responses of the  $\mu Ps$ ,  $v_{i,t}$  and  $v_{r,t}$  primarily represent shear-dominant responses and interfacial friction. Note that the contribution of rotational dynamics is not considered since the rotational energy of the post-impact particle is relatively insignificant compared to the pre-impact kinetic energy. For example, less than 2% of the initial kinetic energy is converted to the rotational energy of the particle having a diameter ( $D_p$ ) of 14.4  $\mu$ m in **Fig. 2b**. The  $\mu$ Ps experience plastic deformation during the impact-rebounding process. While a plastically deformed rebounding  $\mu$ P

immediately after collision is seen in **Fig. 2b**, the plastic deformation is more evident from the retrieved  $\mu P$  in **Fig. 2c**. This large shape change of the  $\mu P$  is indicative of significant kinetic energy dissipation, which will be discussed later.

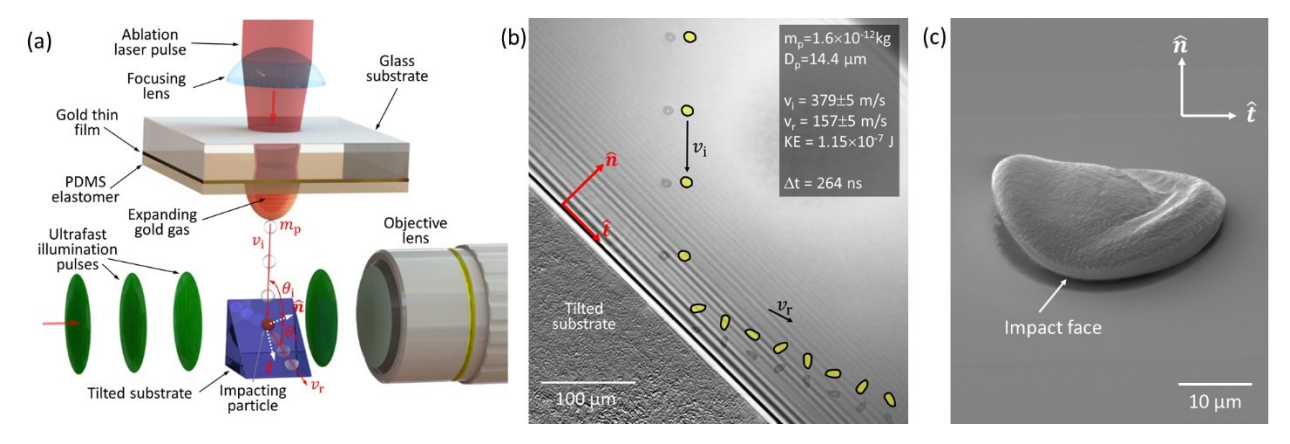


Figure 2. (a) Schematic of θ-LIPIT; (b) An ultrafast stroboscopic image of θ-LIPIT with motion-indicators of a PS87-PDMS40  $\mu$ P during the entire impact-rebounding process. The incident angle of the  $\mu$ P close to 45°, and the rebounding angle is determined by  $v_i$ . Prominent characteristics of the  $\mu$ P during impact are highly inelastic rebounding of the plastically deformed  $\mu$ P along  $\hat{n}$ , sliding with shear and friction-induced rotation along  $\hat{t}$ ; (c) A SEM image of a deformed BCP83-83  $\mu$ P after colliding at  $v_i$ =688 m·s<sup>-1</sup> and  $\theta_i$ =46° shows substantial plastic deformation. The  $\mu$ P rebounding at  $v_r$ =448 m·s<sup>-1</sup> was captured with a soft polymer substrate.

In the relatively low impact velocity  $v_i$  range, below 100 m·s<sup>-1</sup>, the normal rebound velocity  $v_{r,n}$  of PS83  $\mu$ Ps remains proportional to  $v_i$ , but reaches a plateau for impact velocities greater than 100 m·s<sup>-1</sup> (**Fig. 3a**). On the contrary, the tangential component of the rebound velocity  $v_{r,t}$  of PS83 continues to increase linearly beyond 100 m·s<sup>-1</sup>. This consistent linear behavior of  $v_{r,t}$  implies that the interfacial interaction between the PS83  $\mu$ P and the substrate along the tangential direction does not vary significantly with respect to  $v_i$ . However, the saturated  $v_{r,n}$  above 100 m·s<sup>-1</sup> indicates that the compressional deformation becomes highly energy-dissipative, and thus, most kinetic energy associated with the deformation along  $\hat{n}$  is lost except a saturated elastically stored energy, which will be discussed in detail later. The excessive compressive deformation causes a significant plastic flow parallel to  $\hat{t}$ , and localized adiabatic visco-plastic heating elevates the internal temperature of PS83  $\mu$ Ps unevenly.

The response of PS87-PDMS40, a morphology comprised of a glassy matrix with discrete rubbery domains, in **Fig. 3b** is similar to that of PS83, with the exception that  $v_{r,t}$  behavior is slightly nonlinear, indicating a change in the interfacial interaction with  $v_i$ . This nonlinear trend is more profound in the case of PS83-PDMS83 having higher  $f^{PDMS}$  (**Fig. 3c**). For PS83-PDMS83, where it appears that the PDMS block serves as the matrix with PS reinforcement, the fluctuations in  $v_{r,n}$  and  $v_{r,t}$  are wider than the experimental error of 5 m·s<sup>-1</sup>, indicating that the mechanical interaction is potentially affected by a growing instability.

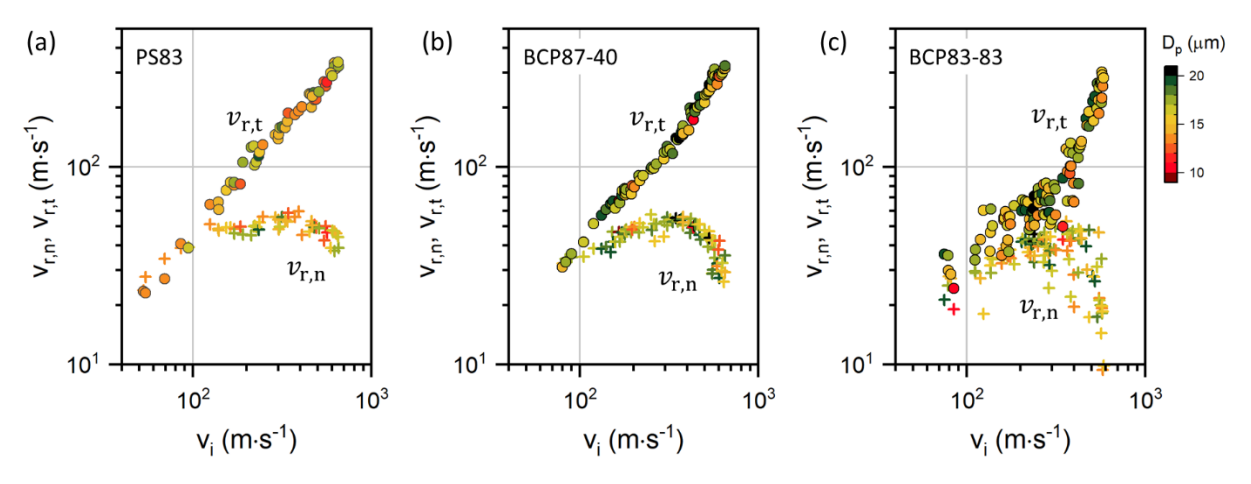


Figure 3 (a) – (c) The  $v_{\rm r,n}$  and  $v_{\rm r,t}$  spectra of PS83, PS87-PDMS40, and PS83-PDMS83  $\mu$ Ps are shown with the common color scale of  $D_{\rm p}$ . All results are from the  $\theta$ -LIPIT with fused silica substrates.

Mass loss from the  $\mu P$  is negligible as evidenced by lack of fragments and an insignificant amount of residue left on the substrate. Therefore, the coefficients of restitution,  $CoR_n$  ( $\equiv v_{r,n}/v_{i,n}$ ) and the  $CoR_t$  ( $\equiv v_{r,t}/v_{i,t}$ ), the normal and tangential coefficients of restitution respectively, are directly related to the change of linear momentum during the interaction of the  $\mu P$  and the substrate. While the total fraction of residual kinetic energy is expressed by  $CoR^2$ , the components,  $CoR_n^2$ , and  $CoR_t^2$  can display the fraction of residual kinetic energy along the surface normal and parallel vectors,  $\hat{n}$  and  $\hat{t}$ , respectively (Fig. 4). The collision process is significantly inelastic, especially for the deformation along  $\hat{n}$  and for higher  $f^{PDMS}$ .  $CoR^2$  has a minimum value due to the non-monotonic trend originating from  $CoR_t^2$ .

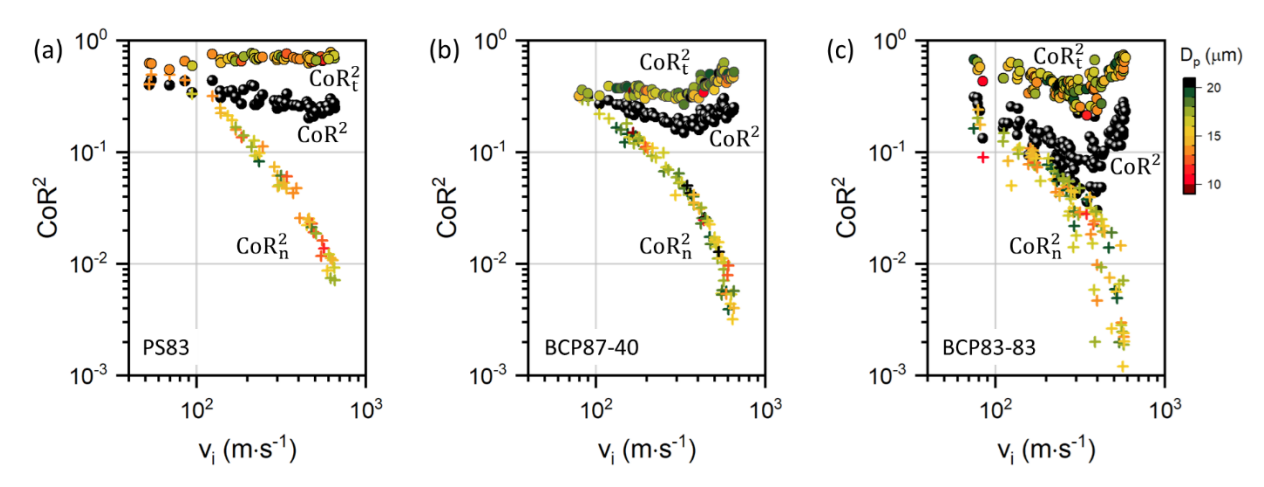


Figure 4 (a) – (c) The  $CoR_n^2$ ,  $CoR_t^2$ , and  $CoR^2$  spectra of PS83, PS87-PDMS40, and PS83-PDMS83 μPs are shown with the common color scale of  $D_p$ . All results are from the θ-LIPIT with fused silica substrates.

The time-averaged force exchanges along  $\hat{n}$  and  $\hat{t}$  can be quantified using  $CoR_n$  and  $CoR_t$ . Using these forces as a normal force and a frictional force, the effective (or time-averaged) coefficient of friction,  $\mu_k^*$ , is quantified by  $^{18}$ :

$$\mu_{k}^{*} = \frac{\nu_{i,t}(1 - CoR_{t})}{\nu_{i,n}(1 + CoR_{n})}.$$
(1)

We propose the effective coefficient of friction  $\mu_k^*$  to be an important measure of UHR tribology of the interface, as the  $CoR_n$  and  $CoR_t$  depend on the collision-induced changes of the intrinsic material properties, such as the phase transition induced by adiabatic heating <sup>13,19,20</sup> at and adjacent to the interface.

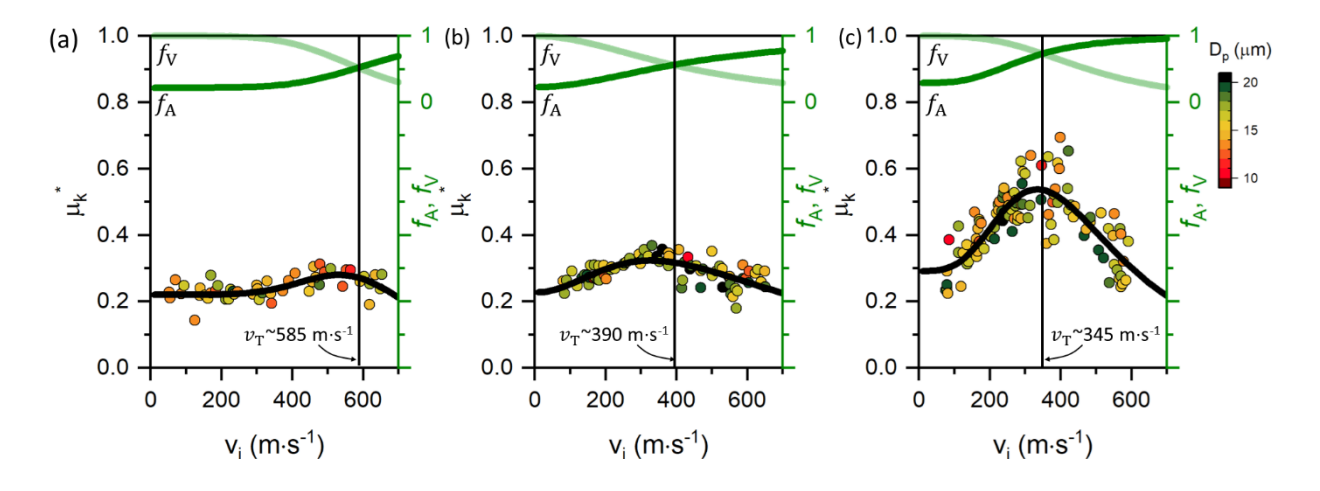


Figure 5 The  $\mu_k^*$  spectra of (a) PS83, (b) PS87-PDMS40, and (c) PS83-PDMS83 μPs are quantified as a function of  $v_i$  spectra, where circular symbols show the experimental values with the common color scale of  $D_p$ . The fitting curves (black) are based on the two functions,  $f_A$  and  $f_V$ , representing the adhesive and viscous effects. All results are from θ-LIPIT with fused silica substrates.

In Fig. 5,  $\mu_k^*$  of PS83 remains nearly constant up to 300 m·s<sup>-1</sup> and then increases to a maximum at  $v_m \sim 530$  m·s<sup>-1</sup>. Independence of  $\mu_k^*$  from the impact speed  $v_i$ , observed when  $v_i < 300$  m·s<sup>-1</sup>, is indicative of the *elastic friction*, where the total normal and tangential force components increase proportionally with increasing contact pressure<sup>21</sup>. Therefore, in this velocity regime the interface is thought to remain as a solid (*solid friction regime*). Since the initial kinetic energies of the  $\mu$ Ps can result in an insignificant temperature rise (< 30 °C) of the entire volume of  $\mu$ P at the onset of increase of  $\mu_k^*$  ( $v_i \geq 300$  m·s<sup>-1</sup>), we hypothesize that the contact surface temperature ( $T_{cont}$ ) of the PS83  $\mu$ P must exceed the impact-induced dynamic glass transition temperature ( $T_g^{PS}$ ) of PS<sup>22</sup> to form a visco-plastic PS layer only near the contact interface. Due to the higher chain mobility of the visco-plastic PS layer, the proportionality between the real area of contact and the apparent contact pressure becomes nonlinear for  $v_i \geq 300$  m·s<sup>-1</sup>. Because the visco-plastic PS-enhanced  $\mu_k^*$  near the interface causes more shear deformation and consequently leads to further thermal softening, reduction of the effective shear viscosity within the visco-plastic PS layer is accelerated. The accelerated softening due to the interaction between adhesion and energy dissipation is reminiscent of the adiabatic shear instability, which has long been studied as an

important bonding mechanism of metallic µPs in cold spray<sup>23</sup> while it is expected in high-rate deformation of polymers.<sup>24</sup> Hence, the non-monotonic trend of  $\mu_k^*$  can be understood as the mobility-enhanced adhesion and adiabatic shear instability originating from the two competing effects: adhesion of polymer to substrate and viscous shear flow within polymer. This nonmonotonic behavior of  $\mu_k^*$  with respect to  $v_i$  is enhanced in the two diblock copolymers with lower  $v_{\rm m}$ ~320 m·s<sup>-1</sup>. Any noticeable difference originating from  $D_{\rm p}$  (10 – 20  $\mu$ m) is not observed in Fig. 5. Moreover, although µPs can be deformed prior to impact due to the inertial compression in the acceleration process, the impact-induced deformation between PS87-PDMS40 and PS83-PDMS83 is not clearly distinguishable (**Fig. S2**). Thus, the greater sensitivity of  $\mu_k^*$  to  $v_i$  of PS83-PDMS83 compared to PS87-PDMS40 suggests that a larger amount of rubbery component and a rubbery matrix (with discrete glassy PS domains) enhances the rheological processes associated with the nonmonotonic behavior. Moreover, due to the lower  $\overline{M}_n^{PDMS}$  in PS87-PDMS40, there are about half as many of entanglements per chain compared to that of PS83-PDMS83<sup>25</sup>. This infers that the material with a glassy matrix has less chain friction than a material with a rubbery matrix which is directly related to  $\mu_k^*$  near the interface as the chain friction determines the resistance force for shear motion of polymers. Since the effective  $T_q$ s of PS83, PS87-PDMS40, and PS83-PDMS83 decreases as  $f^{PDMS}$  increases, the three types of  $\mu Ps$  qualitatively provide the characteristic changes of mechanical responses of polymers when experimental temperature is increased (or effective  $T_q$  is decreased).

**Table 1** Fitting parameters of the  $\mu_k^*$  curves.

Parameters	$\mu_0$	$v_{\rm A}~({\rm m\cdot s^{-1}})$	$v_{\rm V}~({\rm m\cdot s}^{\text{-}1})$	n
PS83 (w/ silica)	0.22±0.01	641±36	596±20	5.1±1.4
PS87-PDMS40	0.23±0.02	445±45	445±23	2.0±0.3
(w/ silica)	0.23±0.02	773273	773123	2.0±0.5
PS83-PDMS83	0.29±0.03	298±14	477±9	3.2±0.3
(w/ silica)	0.27±0.03	270±14	7//1/	3.2±0.3
PS83-PDMS83	0.29	303±12	635±20	3.3±0.3
(w/ sapphire)	0.27	303±12	033±20	3.3±0.3

The non-monotonic character of  $\mu_k^*$  observed in **Fig. 4** is expressed semi-empirically by  $\mu_k^* = f_A f_V$ , where  $f_A$  and  $f_V$  are two functions that represent the adhesive and viscous contributions to  $\mu_k^*$ . These effects are modeled by sigmoid functions,  $\left[1 - \frac{1 - \mu_0}{1 + (v_i/v_A)^{n_1}}\right]$  and  $\left[\frac{1 - \mu_\infty}{1 + (v_i/v_V)^{n_2}} + \mu_\infty\right]$ , where  $v_A$  and  $v_V$  are characteristic velocities for the adhesion and shear phenomena.  $\mu_0$  and  $\mu_\infty$  are the asymptotic values of  $\mu_k^*$  for  $v_i \ll v_A$  and  $v_i \gg v_A$  and  $\mu_\infty \cong 0$  due to shear thinning at high strain rates. Thus, the semi-empirical model for the effective friction coefficient becomes:

$$\mu_{\mathbf{k}}^*(v_{\mathbf{i}}) = \left[1 - \frac{1 - \mu_0}{1 + (v_{\mathbf{i}}/v_{\mathbf{A}})^n}\right] \left[\frac{1}{1 + (v_{\mathbf{i}}/v_{\mathbf{V}})^n}\right]$$
(2)

While introducing a common exponent (n) for both factors to minimize the number of fitting parameters, the nonlinear trend  $\mu_k^*$  is fitted well by Eq. (2) of 4 parameters. The fitted  $\mu_k^*$  spectra and their  $f_A$  and  $f_V$  are shown in **Fig. 5** along with the curve fitting parameters in **Table 1**. We propose a rheological transition velocity ( $v_T$ ), at which  $f_A$  is equal to  $f_V$ , to specify the character of the viscoelastic interfacial response as *solid-like* ( $v_i < v_T$ ) or *liquid-like* ( $v_i > v_T$ ).  $v_T$  systematically shifts from 585 to 345 m·s<sup>-1</sup> as  $f_{PDMS}$  varies from 0 to 30% to 50%. We propose that  $v_T$  can serve as an UHR tribological point, similar to a rheological gel point ( $\tan \delta = 1$ ). Despite the higher  $\overline{M}_n$  of PS-b-PDMS in this study, the liquid-like material at the contact surface of the BCP  $\mu$ P can be phenomenologically similar to the homogeneously mixed liquid layer found around the silica  $\mu$ Ps that supersonically penetrated a bulk PS-b-PDMS lamellar film where the high temperatures and layer compression caused segmental mixing above the order-disorder transition temperature of the BCP.<sup>13</sup>

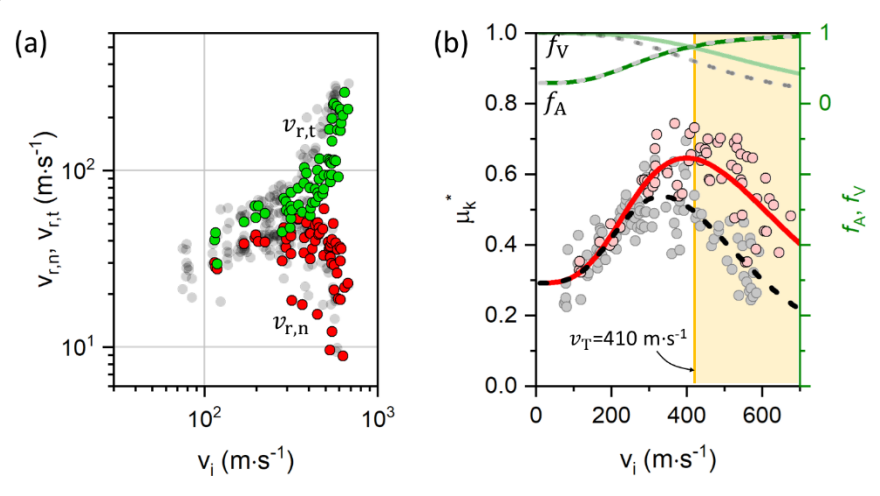


**Figure 6** (a) The  $v_r$  spectra and (b)  $\mu_k^*$  spectra of PS83-PDMS83 of the impact on a single-crystal sapphire (R-plane) substrate are shown (color) with the results from the fused silica substrate (grey) for comparison. The fitting curves from sapphire (red line) and fused silica (black dashed line) substrates show the tribological difference. The adhesive and viscous factors (green curves) represent the rheological characteristics compared to those from fused silica substrate (grey dashed lines).

Table 2 Thermal and surface properties of projectiles and substrate materials<sup>27–30</sup>

	Density, ρ	Specific heat, C <sub>p</sub>	Thermal	Thermal
	$(g/cm^3)$	(J/kgK)	conductivity, Kth	diffusivity,
			(W/mK)	$\alpha = K_{th}/\rho C_p$
PS	1.04-1.065	$1.2 \times 10^6$	0.13	1.02 x 10 <sup>-7</sup> –
				$1.04 \times 10^{-7}$
PDMS	0.974 @ 20°C	1170 - 1460	0.1678 @14.7°C	1.12 x 10 <sup>-7</sup> –
			0.1591 @50°C	$1.47 \times 10^{-7}$
SiO <sub>2</sub>	2.2	772	1.2	8.13 x 10 <sup>-6</sup>
Al <sub>2</sub> O <sub>3</sub>	3.97	787.3 – 782.4	<i>c</i> <sub>⊥</sub> : 30.3	9.69 x 10 <sup>-6</sup> –
			$c_{\parallel}$ : 32.5	10.46 x10 <sup>-6</sup>

According to our hypothesis that the temperature and component dependent adhesion and viscosity effects on  $\mu_k^*$  are related to the contact surface temperature,  $T_{\rm cont}$ , the non-monotonic behavior should be altered as  $T_{\rm cont}$  changes. Although the adiabatic assumption would be valid for most volumes of a  $\mu P$  during the short time scale of the collision (<400 ns), the temperature of the polymer directly contacting the substrate can be affected by heat loss through the contact surface between the  $\mu P$  and the substrate. To lower  $T_{\rm cont}$ , a greater heat loss is introduced at the contact surface by using sapphire substrate ( $C_1$ : 30.3 W/m·K and  $C_{11}$ : 32.5 W/m·K)<sup>29</sup> instead of the fused silica of low thermal conductivity (~1.2 W/m·K)<sup>30</sup> as listed in **Table 2**. Furthermore, the adhesion work between the sapphire substrate and the  $\mu Ps$  is expected to be larger than that between the fused silica and the  $\mu Ps$  due to the larger surface tension of sapphire than fused silica. This can lead to increased  $A_r$  (real contact area) and lead to faster heat loss during impact. As a result, a similar trend of  $v_{r,t}$  appears but is shifted toward the higher range of  $v_i$  in **Fig. 6a**. The change in  $\mu_k^*$  is more pronounced as the maximum of  $\mu_k^*$  increases to ~0.7 and  $v_m$  is noticeably higher (~400)

m·s<sup>-1</sup>) in **Fig. 6b**. As the two  $\mu_k^*$  spectra are not significantly different in the lower range of  $v_i$ ,  $\mu_0$  is assumed to remain almost the same. According to the fitted curve with the parameters in **Table 1**, the adhesion effect (or  $f_A$ ) is nearly unchanged, but the shear thinning effect (or  $f_V$ ) is significantly suppressed. The shift of  $v_T$  from 345 to 410 m·s<sup>-1</sup> supports that the higher thermal loss through the sapphire substrate delays onset of the liquid-like behavior near the interface. Note that  $\overline{M}_n$  is another critical factor that can alter mechanical deformation and rheological characteristics of  $\mu$ Ps since higher  $\overline{M}_n$  increases the entanglement density of polymers. Due to the strong coupling of rheological and tribological characteristics under UHR deformation, the effects originating from  $\overline{M}_n$  cannot be readily predicted and should be investigated through an  $\overline{M}_n$ -controlled study in the future.

### **Conclusion**

In summary, the UHR mechanical and tribological behavior of polymeric μPs with varying ratios of glassy and rubbery components are characterized through the angled collisions in order to decouple the collision dynamics perpendicular and parallel to the contact surface. The compressive plastic flow restrains the material elasticity, and the resultant thermal softening effect from the plastic work increases the adhesive interaction between a µP and the substrate. Due to the interfacial shear instability, the interfacial dynamics exhibit a strong nonlinearity and results in the transition from elastic to viscous friction. The nonlinear transition of the effective friction coefficient is primarily governed by the glassy component of the µP, which produces the thermal softening effect that is inversely proportional to its  $\overline{M}_n$ , chain entanglement, and intermolecular interaction. Although the more rubbery component in BCPs will reduce the static mechanical strength of µPs, the resultant ductility in UHR deformation can amplify interfacial adhesion between the substrate and other µPs, which is desired for the consolidation process of the cold spray additive manufacturing. Since the structural strength of macroscopic additively manufactured products is governed by the coupled function of the μPs' own mechanical strength and its interfacial adhesion strength, the more rubbery component of µPs will not always lead to the deterioration of the structural strength of the final products. As a stepping stone to understanding the complex UHR behavior of polymers, the proposed semi-empirical model based on the effects of adhesion and viscosity is verified by modifying the energy balance in the contact region. This model provides rheological transition rates to classify the basic properties of UHR friction phenomena. Through the demonstrated analysis via  $\theta$ -LIPIT, the UHR tribological nonlinearity originating from simultaneously localized temporal and spatial dimensions can be understood. Moreover, we envision that the rheological properties from theta-LIPIT can provide a standardized measure of polymer feedstock powders predicting cold spray compatibility such as deposition yield and bonding strength.

## **Supporting Information**

The supporting information is available free of charge at https://

Sample preparation and additional characterization results (PDF)

## Acknowledgements

This research was supported by the National Science Foundation under Grant No. CMMI-1760924. JHL and AK gratefully acknowledge A. Avgeropoulos for providing the PS83-PDMS83 block copolymer.

#### References

- (1) Urbakh, M.; Klafter, J.; Gourdon, D.; Israelachvili, J. The Nonlinear Nature of Friction. *Nature* **2004**, *430* (6999), 525–528. https://doi.org/10.1038/nature02750.
- (2) Stachowiak, G. W. How Tribology Has Been Helping Us to Advance and to Survive. *Friction* **2017**, *5* (3), 233–247. https://doi.org/10.1007/s40544-017-0173-7.
- (3) Vakis, A. I.; Yastrebov, V. A.; Scheibert, J.; Nicola, L.; Dini, D.; Minfray, C.; Almqvist, A.; Paggi, M.; Lee, S.; Limbert, G.; Molinari, J. F.; Anciaux, G.; Aghababaei, R.; Echeverri Restrepo, S.; Papangelo, A.; Cammarata, A.; Nicolini, P.; Putignano, C.; Carbone, G.; Stupkiewicz, S.; Lengiewicz, J.; Costagliola, G.; Bosia, F.; Guarino, R.; Pugno, N. M.;

- Müser, M. H.; Ciavarella, M. Modeling and Simulation in Tribology across Scales: An Overview. *Tribol. Int.* **2018**, *125*, 169–199. https://doi.org/10.1016/j.triboint.2018.02.005.
- (4) DePalma, V.; Tillman, N. Friction and Wear of Self-Assembled Trichlorosilane Monolayer Films on Silicon. *Langmuir* **1989**, *5* (3), 868–872. https://doi.org/10.1021/la00087a049.
- (5) Casoli, A.; Brendlé, M.; Schultz, J.; Auroy, P.; Reiter, G. Friction Induced by Grafted Polymeric Chains. *Langmuir* **2001**, *17* (2), 388–398. https://doi.org/10.1021/la0007067.
- (6) Rao, M. P.; Duan, Y.; Keefe, M.; Powers, B. M.; Bogetti, T. A. Modeling the Effects of Yarn Material Properties and Friction on the Ballistic Impact of a Plain-Weave Fabric. *Compos. Struct.* **2009**, *89* (4), 556–566. https://doi.org/10.1016/j.compstruct.2008.11.012.
- (7) Kendall, M.; Mitchell, T.; Wrighton-Smith, P. Intradermal Ballistic Delivery of Micro-Particles into Excised Human Skin for Pharmaceutical Applications. *J. Biomech.* **2004**, *37* (11), 1733–1741. https://doi.org/10.1016/j.jbiomech.2004.01.032.
- (8) Siviour, C. R.; Jordan, J. L. High Strain Rate Mechanics of Polymers: A Review. *J. Dyn. Behav. Mater.* **2016**, *2* (1), 15–32. https://doi.org/10.1007/s40870-016-0052-8.
- (9) Champagne, V. K. *The Cold Spray Materials Deposition Process: Fundamentals and Applications*; Series in Metals and Surface Engineering; Elsevier, 2007.
- (10) Khalkhali, Z.; Xie, W.; Champagne, V. K. V. K.; Lee, J.-H. J.-H.; Rothstein, J. P. J. P. A Comparison of Cold Spray Technique to Single Particle Micro-Ballistic Impacts for the Deposition of Polymer Particles on Polymer Substrates. *Surf. Coatings Technol.* 2018, 351, 99–107.
- (11) Yang, G.; Xie, W.; Huang, M.; Champagne, V. K. V. K.; Lee, J.-H. H. J.-H.; Klier, J.; Schiffman, J. D. J. D. Polymer Particles with a Low Glass Transition Temperature Containing Thermoset Resin Enable Powder Coatings at Room Temperature. *Ind. Eng. Chem. Res.* **2019**, *58* (2), 908–916. https://doi.org/10.1021/acs.iecr.8b04698.
- (12) Hyon, J.; Gonzales, M.; Streit, J. K.; Fried, O.; Lawal, O.; Jiao, Y.; Drummy, L. F.; Thomas, E. L.; Vaia, R. A. Projectile Impact Shock-Induced Deformation of One-Component

- Polymer Nanocomposite Thin Films. *ACS Nano* **2021**. https://doi.org/10.1021/acsnano.0c06146.
- (13) Lee, J.-H.; Veysset, D.; Singer, J. P.; Retsch, M.; Saini, G.; Pezeril, T.; Nelson, K. A.; Thomas, E. L. High Strain Rate Deformation of Layered Nanocomposites. *Nat. Commun.* **2012**, *3* (May), 1164. https://doi.org/10.1038/ncomms2166.
- (14) Lee, J.-H.; Loya, P. E.; Lou, J.; Thomas, E. L. Dynamic Mechanical Behavior of Multilayer Graphene via Supersonic Projectile Penetration. *Science* (80-. ). **2014**, 346 (6213), 1092–1096. https://doi.org/10.1126/science.1258544.
- (15) Xie, W.; Alizadeh-Dehkharghani, A.; Chen, Q.; Champagne, V. K.; Wang, X.; Nardi, A. T.; Kooi, S.; Müftü, S.; Lee, J.-H. Dynamics and Extreme Plasticity of Metallic Microparticles in Supersonic Collisions. *Sci. Rep.* 2017, 7 (1), 5073. https://doi.org/10.1038/s41598-017-05104-7.
- (16) Panagiotou, T.; Levendis, Y. A. Generation of Spherical and Monodisperse Particles of Poly(Styrene) and Poly(Methyl Methacrylate) by Atomization of Monomers and Dissolved Polymer Precursors. *J. Appl. Polym. Sci.* **1991**, *43* (8), 1549–1558. https://doi.org/10.1002/app.1991.070430818.
- (17) Bates, F. S. Polymer-Polymer Phase-Behavior. *Science* (80-. ). **1991**, 251 (4996), 898–905. https://doi.org/DOI 10.1126/science.251.4996.898.
- (18) Sondergaard, R.; Chaney, K.; Brennen, C. E. Measurements of Bouncing Off Flat Plate. *J. Appl. Mech.* **1990**, *112* (90), 694–699.
- (19) R.H.O. Frictional Properties of Rubber. *J. Franklin Inst.* **1942**, *233* (5), 486–487. https://doi.org/10.1016/s0016-0032(42)90630-6.
- (20) Friedrich, K. Polymer Composites for Tribological Applications. *Adv. Ind. Eng. Polym. Res.* **2018**, *I* (1), 3–39. https://doi.org/10.1016/j.aiepr.2018.05.001.
- (21) F. P. BOWDEN, D. T. Mechanism of Metallic Friction. *Nat. No. 3798, August 15, 1942*1942, No. 3798, 197–199.

- (22) Sun, Y.; Kooi, S. E.; Nelson, K. A.; Hsieh, A. J.; Veysset, D. Impact-Induced Glass-to-Rubber Transition of Polyurea under High-Velocity Temperature-Controlled Microparticle Impact. *Appl. Phys. Lett.* **2020**, *117* (2), 021905. https://doi.org/10.1063/5.0013081.
- (23) Grujicic, M.; Zhao, C. L.; DeRosset, W. S.; Helfritch, D. Adiabatic Shear Instability Based Mechanism for Particles/Substrate Bonding in the Cold-Gas Dynamic-Spray Process. *Mater. Des.* **2004**, *25* (8), 681–688. https://doi.org/10.1016/j.matdes.2004.03.008.
- (24) Fleck, N. A. Adiabatic Shear Instability: Theory; Springer, Dordrecht, 1999. https://doi.org/10.1007/978-94-015-9231-4\_4.
- (25) Fetters, L. J.; Lohse, D. J.; Richter, D.; Witten, T. A.; Zirkel, A. Connection between Polymer Molecular Weight, Density, Chain Dimensions, and Melt Viscoelastic Properties. *Macromolecules* **1994**, *27* (17), 4639–4647. https://doi.org/10.1021/ma00095a001.
- (26) Donley, G. J.; de Bruyn, J. R.; McKinley, G. H.; Rogers, S. A. Time-Resolved Dynamics of the Yielding Transition in Soft Materials. *J. Nonnewton. Fluid Mech.* **2019**, *264*, 117–134. https://doi.org/10.1016/j.jnnfm.2018.10.003.
- (27) Contents, S.; Class, P. Polymer Data; 1999.
- (28) Harper, C. A. Handbook of Ceramics, Glasses and Diamonds; 2001.
- (29) Dobrovinskaya, E. R. *Sapphire: Material, Manufacuting, Applications*; Springer International Publishing, 2009. https://doi.org/0.1007/978-0-387-85695-7.
- (30) Wray, K. L.; Connolly, T. J. Thermal Conductivity of Clear Fused Silica at High Temperatures. *J. Appl. Phys.* **1959**, *30* (11), 1702–1705. https://doi.org/10.1063/1.1735040.

# **Table of Contents (TOC) graphic**

